21st Australasian Fluid Mechanics Conference
Adelaide, Australia
10-13 December 2018

Autonomous Propulsion of Nanorods Trapped in an Acoustic Field

J. E. Sader, J. F. Collis and D. Chakraborty

ARC Centre of Excellence in Exciton Science
School of Mathematics and Statistics
The University of Melbourne
Victoria 3010, Australia

Abstract

Acoustic fields in a liquid medium can trap and suspend small particles at their pressure nodes. Recent measurements demonstrate that nanorods immersed in these fields generate autonomous propulsion, with their direction and speed controlled by both the particle's shape and density distribution. In this talk, we investigate the physical mechanisms underlying this combined density/shape induced phenomenon by developing a simple yet rigorous mathematical framework for axisymmetric particles. This shows that geometric and density asymmetries in the particle generate axial jets that can produce motion in either direction, depending on the relative strengths of these asymmetries and the acoustic Reynolds number. Strikingly, the propulsion direction is found to reverse with increasing frequency, an effect that is yet to be reported experimentally. The general theory and mechanism described here enable the *a priori* design and fabrication of nano-motors in fluid for transport of small-scale payloads and robotic applications.

Introduction

Synthetic (non-biological) nanoscale motors have been developed for applications in the biological sciences, including transport of colloidal cargos [12, 18], chemical analysis of pollutants [5, 9] and detection of DNA and other biological molecules [16, 3]. These motors can also produce emergent dynamics when gathered in large ensembles. Swarming and hydrodynamic synchronisation are but a few of the intriguing dynamics that occur in these systems [6, 17].

Measurements show that individual nano and micrometre scale rods can produce *autonomous propulsion* in acoustic fields [13], i.e., the particles themselves actively generate their propulsive motion rather than being moved passively by an external steady flow. These rods migrate towards a pressure node in a standing acoustic wave where they subsequently exhibit a variety of dynamics, including aggregation, random walks and orbital motion [1, 2, 10, 14, 15]. These motors offer a distinct advantage over the autonomous motion of catalytic devices because chemical fuels, which are toxic to many biological systems, are not used. In addition, acoustic fields in the MHz range have been applied extensively in biologically sensitive environments with minimal adverse impact [7].

In the above-described measurements, nanorods composed of a single metal are always observed to move with their concave end leading [13]. More recent measurements [2] show that shape and density asymmetries can produce competing effects, with the particle tending to propel itself with its low density and concave end leading the motion.

In this study, we formulate a general theoretical framework for this phenomenon that can be used to explain its essential physical mechanisms [4]. Previously used assumptions of a nearly-spherical and homogeneous density particle in a low acoustic Reynolds number flow [8] are relaxed. The developed framework is applicable to arbitrarily shaped axisymmetric solids with arbitrary density distributions that are driven at arbitrary finite frequency. Application to a simple particle, a dumbbell consisting of two well-separated spheres, is considered allowing the essential physical mechanisms underlying propulsion to be explored. The general framework is then implemented numerically for asymmetric nanorods that resemble the shape of the particles reported in measurements. The effects of shape and density asymmetries are illustrated and discussed.

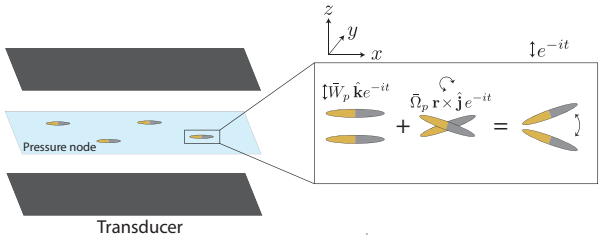

Figure 1: Schematic of acoustic chamber bounded by upper and lower panels, used to trap particles which exhibit autonomous propulsion. Particles migrate to the pressure node/velocity antinode at the chamber.'s centre Inset: Particle motion is generally decomposed into linear and angular components.

General Theoretical Framework

A schematic of the measurement protocol of [1, 2, 13] is given in figure 1. The particle aligns itself perpendicular to this imposed flow [2]. The origin of the Cartesian coordinate system is chosen to be the particle's geometric centre. The following set of scales is used: all velocities are scaled by the velocity amplitude of the applied oscillatory flow (at the pressure node), U, time by the reciprocal of the angular frequency of the imposed flow, $1/\omega$, the hydrodynamic length scale is R (radius along the particle's minor axis), pressure is scaled by $\mu U/R$ (for convenience only) and hence force by μUR, where μ is the fluid's shear viscosity; the Lagrangian displacement amplitude of the fluid is $a = U/\omega$. From this point forward, all variables shall refer to their dimensionless quantities.

The non-dimensional Navier-Stokes equations are

$$\nabla\cdot\mathbf{u} = 0, \qquad \beta\frac{\partial\mathbf{u}}{\partial t} + \varepsilon\beta\mathbf{u}\cdot\nabla\mathbf{u} = -\nabla p + \nabla^2\mathbf{u}, \qquad (1)$$

where $\mathbf{u}$ is the velocity field of the fluid, p is the fluid pressure, t is time, the acoustic Reynolds number is $\beta \equiv \rho R^2\omega/\mu$, the dimensionless oscillation amplitude is $\varepsilon \equiv a/R \ll 1$ and ρ is the fluid density. We use the explicit time dependence, $\exp(-it)$, for the imposed acoustic velocity, where i is the imaginary unit; the true velocities of the fluid and particle (as measured) are specified here by the real part.

The boundary conditions for the fluid velocity are $\mathbf{u} \to e^{-it}\hat{\mathbf{k}}$ as $|\mathbf{r}| \to \infty$, and $\mathbf{u} = \mathbf{U}_p$ on $\mathbf{r} \in S_p$, where the position vector, $\mathbf{r}$, is specified in the Cartesian frame of figure 1. S_p denotes

the surface of the particle and $\mathbf{U}_p$ is the unknown (to be determined) particle velocity.

Asymptotic expansions of the fluid and particle motion are performed in the small-amplitude parameter, ε, which quantifies the difference between the Lagrangian and Eulerian accelerations (that generates the particle propulsion), giving,

$$\mathbf{u} = \mathbf{u}^{(0)} + \varepsilon \mathbf{u}^{(1)} + o(\varepsilon), \tag{2}$$

and similarly for p and $\mathbf{U}_p$, where the superscripts indicate the order of each term. The fluid and particle motion in the zero-amplitude limit are specified by the leading-order terms.

Leading-Order Flow and Particle Motion

The leading-order flow in equation (2), i.e., of $O(1)$, satisfies

$$\nabla \cdot \bar{\mathbf{u}}^{(0)} = 0, \quad -i\beta \bar{\mathbf{u}}^{(0)} = -\nabla \bar{p}^{(0)} + \nabla^2 \bar{\mathbf{u}}^{(0)}, \tag{3}$$

which are to be solved subject to the far field oscillatory flow and no-slip at the particle's surface. Fourier components of all variables, which depend only on the spatial coordinates and acoustic Reynolds number – not time – are denoted with an over-score, e.g., $p^{(0)} = \bar{p}^{(0)} e^{-it}$.

Due to linearity, the unsteady Stokes solution is at the same frequency as the far field boundary condition. Given the particle's axisymmetry, the corresponding leading-order motion of the (unrestrained) particle admits the general form,

$$\mathbf{U}_p^{(0)} = \left(\bar{W}_p \hat{\mathbf{k}} + \bar{\Omega}_p \mathbf{r} \times \hat{\mathbf{j}}\right) e^{-it}, \tag{4}$$

where the symbols $\bar{W}_p$ and $\bar{\Omega}_p$ denote the linear and angular rigid-body velocities of the particle about its geometric centre. Conservation of linear and angular momentum then leads to the required governing equations [4], which can be readily solved for $\bar{W}_p$ and $\bar{\Omega}_p$.

First-Order Flow and Propulsion Velocity

The steady first-order flow, i.e., at $O(\varepsilon)$, is incompressible and satisfies

$$-\nabla \bar{p}^{(1)} + \nabla^2 \bar{\mathbf{u}}^{(1)} = \frac{\beta}{4}\left(\bar{\mathbf{u}}^{(0)} \cdot \nabla \bar{\mathbf{u}}^{(0)*} + \bar{\mathbf{u}}^{(0)*} \cdot \nabla \bar{\mathbf{u}}^{(0)}\right), \tag{5}$$

where starred quantities denote the complex conjugate. The unsteady contribution to the first-order velocity field has a time-averaged value of zero, and is therefore irrelevant to propulsion.

Calculation of the required first-order flow is performed using the Lorentz reciprocal theorem, employing an auxiliary flow, $\mathbf{u}'$, of the particle translating with uniform velocity in the direction its axis is aligned. This gives the required result for the particle's propulsion velocity, $\mathbf{U}_{\text{prop}} = U_{\text{prop}}\hat{\mathbf{i}}$, where

$$U_{\text{prop}} = \frac{\beta}{4F_p} \iiint_V \mathbf{u}' \cdot \left(\bar{\mathbf{u}}^{(0)} \cdot \nabla \bar{\mathbf{u}}^{(0)*} + \bar{\mathbf{u}}^{(0)*} \cdot \nabla \bar{\mathbf{u}}^{(0)}\right) \mathrm{d}V. \tag{6}$$

Here, $\mathbf{F}_p = F_p \hat{\mathbf{i}}$ is the hydrodynamic drag force on the particle moving with unitary velocity along its symmetry axis, i.e., $\mathbf{U}_p = \hat{\mathbf{i}}$. The result in equation (6) provides the generalisation of that previous result to any axisymmetric particle operating at arbitrary frequency. The *dimensional* propulsion velocity of the particle is $\left(a^2\omega/R\right)U_{\text{prop}}\hat{\mathbf{i}}$.

Application to a Dumbbell-Shaped Particle

We now apply the above general theory to a slender axisymmetric particle and explore the physical mechanisms underlying the particle propulsion observed experimentally in [1, 2, 13]. Density variations and shape asymmetries in the particle are included. To facilitate analytical solution, while capturing the dominant features of the reported experiments, a slender dumbbell consisting of two rigidly connected spheres of (dimensional) radii R_1 and R_2 is chosen.

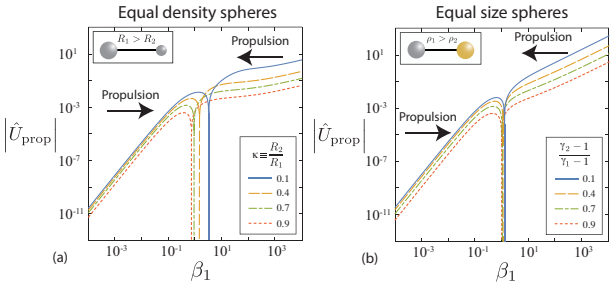

Figure 2: Propulsion velocity of dumbbell-shaped particles as a function of acoustic Reynolds number of Sphere 1, β_1, where the aspect ratio dependence is scaled out of the solution, i.e., $U_{\text{prop}} = \hat{U}_{\text{prop}}/A$. Density of Sphere 1 is held constant (at $10\times$ the value of the fluid, i.e., $\gamma_1 = 10$). (a) Densities of the two spheres are constant and identical. (b) Sizes of both spheres are held constant with $\kappa \equiv R_2/R_1 = 1$.

The dumbbell is aligned in the x-direction such that Sphere 2 has a larger x-coordinate relative to Sphere 1; see insets of figure 2. The chosen length scale for the problem is the radius of Sphere 1, R_1, such that the non-dimensional radius of Sphere 2 is

$$\kappa \equiv \frac{R_2}{R_1}. \tag{7}$$

The nondimensional densities of Spheres 1 and 2 are

$$\gamma_n \equiv \frac{\rho_n}{\rho}, \tag{8}$$

with $n = 1, 2$ corresponding to the two spheres. The radii of the spheres are much smaller than their separation, i.e., the aspect ratio $A \equiv L/R_1 \gg 1$, where L is the separation distance between the centres of the two spheres. This enables independent calculation of the hydrodynamic loads that they experience, i.e., the spheres do not interact hydrodynamically.

Spheres of Identical Density

To begin, we consider the case where the dumbbell's spheres have identical density, i.e., $\gamma_1 = \gamma_2$. Figure 2(a) presents numerical results for the propulsion velocity where the radius of Sphere 1 is held constant and that of Sphere 2 is varied, such that $R_2 > R_1$ (i.e., $\kappa > 1$). The density of the spheres is $10\times$ greater than that of the fluid in this example. Results for other density ratios show similar trends.

The dumbbell is observed to move with the smaller Sphere 2 leading the motion at low acoustic Reynolds numbers, β_1, whereas the larger Sphere 1 leads at high acoustic Reynolds numbers; as illustrated in figure 2(a). That is, the motion reverses at intermediate acoustic Reynolds number. This behaviour is not unexpected because propulsion is driven by a streaming flow—where flow in the viscous boundary layer is typically opposite in sign to that far from the surface, as demonstrated for a sphere executing translational oscillations [11]. Increasing β_1 decreases the viscous penetration depth and confines vorticity closer to the particle's surface. As such, the auxiliary Stokes field, $\mathbf{u}'$, in equation (6) samples a different region of the convective body force. We also observe that decreasing

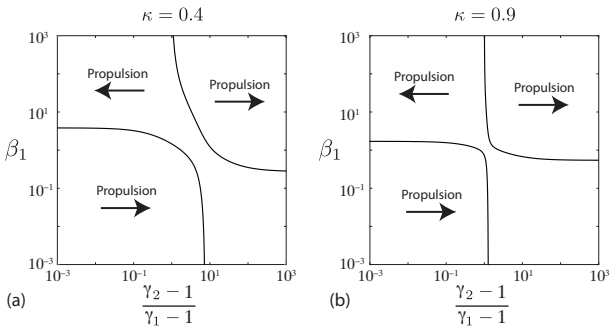

Figure 3: Phase diagrams of a dumbbell-shaped particle's propulsion direction as a function of its density asymmetry and the acoustic Reynolds number of Sphere 1, β_1. Results given for $\gamma_1 = 10$. Sphere radius ratios of (a) $\kappa = 0.4$, (b) $\kappa = 0.9$.

the radius of Sphere 2, i.e., increasing the amount of asymmetry in the particle, enhances the propulsion velocity.

Each sphere executes translational (in the vertical direction) and rotational oscillations; the latter being generated by the spheres' rigid-body coupling. Sphere 2 possesses less inertia than Sphere 1 and thus exhibits a larger vertical velocity amplitude relative to the fixed Cartesian frame. The leading-order flows of the spheres do not interact hydrodynamically in the large aspect ratio limit considered here, $A \gg 1$, and interaction of their resulting (individual) streaming flows does not lead to propulsion at $O(1/A)$; which is the leading-order scaling behaviour with aspect ratio. Propulsive motion of the dumbbell is therefore due to two independent and tandem sphere "engines" that work cooperatively to generate propulsion in the same direction.

Spheres of Identical Radii

We study the complementary situation where the dumbbell's spheres have identical radii, i.e., $\kappa = 1$, but different mass densities. Figure 2(b) presents numerical results where the density of Sphere 1 is held constant ($10\times$ that of the fluid) and the density of Sphere 2 is decreased so that $\gamma_1 > \gamma_2$; results for other density ratios (between Sphere 1 and the fluid) show similar trends.

It is observed that Sphere 2 leads the motion for low acoustic Reynolds numbers, β_1, i.e., the sphere of smaller density. In contrast, the sphere of greater density, Sphere 1, leads at high acoustic Reynolds numbers. The reason for this behaviour is identical to that given in the previous section. The sphere with the larger vertical amplitude leads the propulsion at low acoustic Reynolds number and the sphere with the smaller vertical amplitude at high acoustic Reynolds number.

We thus conclude that both density and shape asymmetries generate propulsion, potentially in opposing directions. Interplay between these geometric and density effects is now explored.

Combination of density and shape asymmetries

Particle behaviour when combining shape and density asymmetries is shown in figure 3. The curves in these phase space diagrams correspond to a propulsion velocity of zero, and delineate regions of different directional motion; these are henceforth termed "zero-propulsion curves". The interplay between density and shape asymmetries is highly nonlinear, which may be expected because propulsion is generated by a streaming flow. We find that particles are able to change direction either once or twice with increasing acoustic Reynolds number, β_1, depending on the relative strength of the shape and density asymmetries. This feature is not unexpected because the acoustic Reynolds

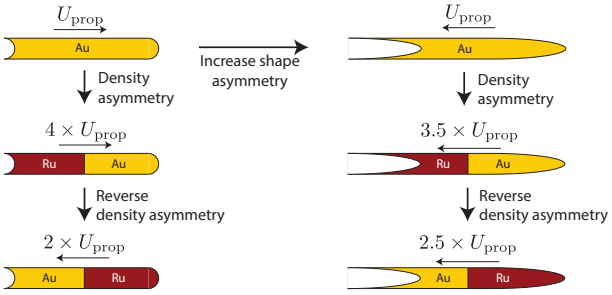

Figure 4: Propulsion directions and relative speeds for asymmetric nanorods operating at $\beta = 0.53$. Left-hand column: hemi-spherically capped nanorods. Right-hand column: hemi-spheroidally capped nanorods.

number where the particle exhibits a zero-propulsion velocity can be different for density and shape asymmetries; see figure 2.

This highlights an important design criterion for robust operation: these nano-motors should be operated far away from any zero propulsion curve, i.e., either at low or high acoustic Reynolds numbers and with either a strong shape or density asymmetry.

Nanorod Propulsion Measurements Reported in [2]

Measurements reported in [2] used nanorods of nominal length of 2 μm (varying in the range of 1.6-2.6 μm, with an uncertainty of $\pm 10\%$) and a diameter of 300 ± 30 nm. These were performed in an acoustic cell formed from two flat plates, separated by 180 μm. Water was confined between the plates; temperature was not reported so we choose a nominal value of 20°C. The lower plate was oscillated vertically using a piezoelectric transducer at 3.77 MHz. The acoustic Reynolds number is therefore $\beta = 0.53 \pm 0.16$, based on the reported nanorod radii. That is, all experiments were conducted close to the theoretically predicted zero-propulsion point. This complicates a comparison with theory, since the precise particle shapes were not characterised.

We therefore resort to a qualitative comparison, where the particle ends are modelled as hemi-spheroids. and we systematically vary the concavity of the ends and change the nature of the density asymmetries. All calculations are performed numerically in COMSOL by first computing the leading-order flow, following which the propulsion velocity is determined using equation (6).

Consider a nanorod with a shape asymmetry defined by hemi-spherical caps and composed only of Au; see upper left schematic of particle in figure 4. While [2] report that the concave end always leads the propulsion of a particle composed of a single material, we find the opposite behaviour: the convex end leads. Since $\beta = 0.53 \sim O(1)$, changes in particle shape can potentially affect the propulsion direction. This is borne out in simulations, where increasing the concavity of the ends reverses the propulsion direction; see upper right schematic in figure 4.

To assess the general trends reported by [2], density asymmetries are introduced to the homogenous density nanorods studied above. Replacing the material of the hemi-spherically capped nanorod with RuAu strongly increases its propulsion velocity, but with the opposite trend to that reported by [2]. Reversing the composition to AuRu reverses the motion. As such, the heavy end of the nanorod leads the propulsion direction rather than the light end. In contrast, the nanorod with large concavity (hemi-spheroidal caps) exhibits the opposite behaviour. This is somewhat similar to the general trends described by [2], though the enhanced propulsion velocity of the

AuRu nanorod relative to the single material Au nanorod is not anticipated from experiments.

These simulations show that the trends reported by [2] provide a small glimpse into the complex behaviour of these nanorods. Further measurements for a range of shape and density asymmetries provides an interesting avenue for future work.

Conclusions

We have studied the steady autonomous propulsion generated by nanorods trapped in an acoustic field. A general theoretical framework for an arbitrary axisymmetric particle was developed that enables its propulsion velocity to be calculated from the unsteady Stokes flow generated by the particle. The particle can possess both geometric and density asymmetries of an arbitrary nature and the acoustic field can be operated at any frequency. This generalises previous work by [8] who studied nearly-spherical particles with shape asymmetries only that are driven at low frequency.

This general framework was applied to slender dumbbell-shaped particles, from which the physical mechanisms were uncovered. This showed that operation at intermediate acoustic Reynolds number, i.e., $\beta \sim O(1)$, can lead to propulsion in either direction which depends sensitively on the particle details. The general framework was then applied to investigate the nanorod system studied experimentally by [2]. Simulations showed that changing the concavity of the model particles that mimic the structure of the experimental system can dramatically alter the particle motion. These findings are yet to be reported in measurements.

This study provides insight into the interplay of density and shape asymmetries and enables the *a priori* design and characterisation of these autonomous acoustic motors.

Acknowledgements

The authors gratefully acknowledge support of the ARC Centre of Excellence in Exciton Science (CE170100026), the Australian Research Council Grants Scheme and an Australian Postgraduate Award.

References

[1] Ahmed, S., Gentekos, D. T., Fink, C. A. and Mallouk, T. E., Self-assembly of nanorod motors into geometrically regular multimers and their propulsion by ultrasound, *ACS Nano*, **8**, 2014, 11053–11060.

[2] Ahmed, S., Wang, W., Bai, L., Gentekos, D. T., Hoyos, M. and Mallouk, T. E., Density and shape effects in the acoustic propulsion of bimetallic nanorod motors, *ACS Nano*, **10**, 2016, 4763–4769.

[3] Campuzano, S., Kagan, D., Orozco, J. and Wang, J., Motion-driven sensing and biosensing using electrochemically propelled nanomotors, *Analyst*, **136**, 2011, 4621–4630.

[4] Collis, J. F., Chakraborty, D. and Sader, J. E., Autonomous propulsion of nanorods trapped in an acoustic field, *J. Fluid Mech.*, **825**, 2017, 29–48.

[5] Guix, M., Orozco, J., García, M., Gao, W., Sattayasamitsathit, S., Merkoçi, A., Escarpa, A. and Wang, J., Superhydrophobic alkanethiol-coated microsubmarines for effective removal of oil, *ACS Nano*, **6**, 2012, 4445–4451.

[6] Ibele, M., Mallouk, T. E. and Sen, A., Schooling behavior of light-powered autonomous micromotors in water, *Angew. Chem. Int. Ed.*, **48**, 2009, 3308–3312.

[7] Litvak, E., Foster, K. R. and Repacholi, M. H., Health and safety implications of exposure to electromagnetic fields in the frequency range 300 Hz to 10 MHz, *Biolelectromag*, **23**, 2002, 68–82.

[8] Nadal, F. and Lauga, E., Asymmetric steady streaming as a mechanism for acoustic propulsion of rigid bodies, *Phys. Fluids*, **26**, 2014, 082001.

[9] Orozco, J., García-Gradilla, V., D'Agostino, M., Gao, W., Cortés, A. and Wang, J., Artificial enzyme-powered microfish for water-quality testing, *ACS Nano*, **7**, 2013, 818–824.

[10] Rao, K. J., Li, F., Meng, L., Zheng, H., Cai, F. and Wang, W., A force to be reckoned with: a review of synthetic microswimmers powered by ultrasound, *Small*, **11**, 2015, 2836–2846.

[11] Riley, N., On a sphere oscillating in a viscous fluid, *Quart. J. Mech. Appl. Math.*, **19**, 1966, 461–472.

[12] Sundararajan, S., Lammert, P. E., Zudans, A. W., Crespi, V. H. and Sen, A., Catalytic motors for transport of colloidal cargo, *Nano Lett.*, **8**, 2008, 1271–1276.

[13] Wang, W., Castro, L. A., Hoyos, M. and Mallouk, T. E., Autonomous motion of metallic microrods propelled by ultrasound, *ACS Nano*, **6**, 2012, 6122–6132.

[14] Wang, W., Duan, W., Zhang, Z., Sun, M., Sen, A. and Mallouk, T. E., A tale of two forces: simultaneous chemical and acoustic propulsion of bimetallic micromotors, *Chem. Comm.*, **51**, 2015, 1020–1023.

[15] Wang, W., Li, S., Mair, L., Ahmed, S., Huang, T. J. and Mallouk, T. E., Acoustic propulsion of nanorod motors inside living cells, *Angew. Chem. Int. Ed.*, **53**, 2014, 3201–3204.

[16] Wu, J., Balasubramanian, S., Kagan, D., Manesh, K. M., Campuzano, S. and Wang, J., Motion-based DNA detection using catalytic nanomotors, *Nature Comm.*, **1**, 2010, 36.

[17] Xu, T., Soto, F., Gao, W., Dong, R., Garcia-Gradilla, V., Magaña, E., Zhang, X. and Wang, J., Reversible swarming and separation of self-propelled chemically powered nanomotors under acoustic fields, *J. Am. Chem. Soc.*, **137**, 2015, 2163–2166.

[18] Ye, Z., Diller, E. and Sitti, M., Micro-manipulation using rotational fluid flows induced by remote magnetic micromanipulators, *J. Appl. Phys.*, **112**, 2012, 064912.